KNOWLEDGE-BASED TURBINE DISK MODELING – A CONCEPTUAL DESIGN PROCESS CALIBRATED TO THE NASA ENERGY EFFICIENT ENGINE

Patrick Wehrel[1], Jens Schmeink[1], Jannik Häßy[1]

[1]German Aerospace Center (DLR), Institute of Propulsion Technology

Abstract

Turbomachinery disks are highly stressed components that contribute significantly to the overall engine mass. Therefore, disk design is crucial and should be already considered in the early phase of conceptual design. In order to advance this field of engineering, this paper proposes a preliminary design process for turbomachinery disks. The process includes the knowledge-based modeling of disk geometries with subsequent mass prediction. Since the temperature has a substantial impact on the material properties and the occurring mechanical stresses, a novel approach for estimating the disk material temperature is also presented. Finally, a stress and burst analysis is performed to evaluate the structural disk integrity. To ensure that the conceptual design process generates reliable results, it is calibrated based on the high- and low-pressure turbine of the NASA Energy Efficient Engine (E3). This additionally enables the determination of knowledge-based design parameters for turbine disks as well as the assessment of safety factors used in stress and burst analysis.

Keywords: conceptual design, disk, geometry, stress, turbine

1. Introduction

Rotating disks are essential components of every turbomachinery, since they transfer the torque between the rotor blades and the shaft. According to *Reed* [1], the disks accounts for approximately 20 % of the total weight and roughly 10 % of the economic value of a civil engine. Therefore, turbomachinery disk design is crucial and should be already considered in the early phase of conceptual design [2-5]. Preliminary disk modeling is a highly challenging task, as there are usually many uncertainties that engineers have to face, but accurate predictions are required nonetheless. Especially the tradeoff between disk mass and life time is a critical aspect that has to be handled carefully [2,3].

In order to facilitate this task for engineers, this paper provides knowledge-based design parameters for turbine disks which are derived from the NASA Energy Efficient Engine (E3). Performance and geometry models are generated for the high- and low-pressure turbine of the NASA E3 and a conceptual disk design process is calibrated based on these models. Although the developed process has a low fidelity compared to finite element method simulations, it enables the rapid analysis of large design spaces and thus the identification of a reasonable starting point for more detailed investigations. Nevertheless, the calibration performed in this paper ensures that the process generates reliable results even in the early phase of conceptual design. To the authors' knowledge, the calibration of a preliminary design process for turbomachinery disks based on the high- and low-pressure turbine of the NASA E3 is unique in the literature. Moreover, a novel approach for estimating the disk material temperature is presented.

Several contributions on conceptual disk design have been published in recent decades. Already in the 1970s, General Electric (GE) carried out studies on a high-pressure turbine disk of the CF6-50 turbofan engine considering disk stress and low cycle fatigue lifetime [6]. In the 1990s, *Armand* [2] presented a structural design methodology for disks which was implemented in a computer program and validated using the 10th stage high-pressure compressor disk of the NASA E3. An important

contribution was published in 2004 by *Tong et al.* [3] who improved disk mass calculation and incorporated a disk stress and lifetime approach into a conceptual design tool. More recent studies have been carried out by *Gutzwiller et al.* [4] as well as *Kolias et al.* [5]. *Gutzwiller et al.* developed a rapid low fidelity turbomachinery disk optimization process and *Kolias et al.* presented a preliminary mechanical design tool for gas turbine disks which was also validated based on the high-pressure compressor of the NASA E3.

2. Reference Turbine Models

The NASA Energy Efficient Engine (E3) of Pratt & Whitney (P&W) [7] is used as reference for the calibration of a conceptual disk design process in this paper. This engine was developed under the NASA E3 program in the 1970s in response to the energy crisis and the rapidly increasing fuel prices [8]. As part of the NASA E3 program, the research and test results were published in a series of detailed reports that have become well-established in academia. Since this paper focuses on turbine disk modeling, the design reports of P&W's high-pressure turbine (HPT) and low-pressure turbine (LPT) are used as main literary source [9,10]. Correspondingly, all models applied in this work are created based on these reports.

The reference models of P&W's NASA E3 HPT and LPT are generated by using the framework GTlab (Gas Turbine Laboratory) developed by DLR [11]. Figure 1 illustrates the performance models of the single-stage HPT and the four-stage LPT which are created by means of the GTlab performance module. Additionally, important turbine performance data is listed in Table 1. Since this work focuses the HPT and LPT of P&W's NASA E3 and sufficient data is available in the corresponding reports, only the turbines and not the entire engine are modeled. The HPT model is generated in a comprehensive design process reported in [12,13]. Subsequently, the thermodynamic LPT model is designed based on the same modeling approach (note that the four-stage LPT is modeled as an equivalent single-stage turbine [14]). The performance models are briefly described below, details are provided in [12]. As in the NASA E3 design reports, both models are designed for cruise conditions (CR). The highest shaft speeds are reported at takeoff (TO), which is therefore an important off-design point for disk modeling. Basically, both models consist of the respective turbine that is connected through a shaft to a generator consuming the turbine power. Cooling and sealing air is provided by the secondary air system (SAS) to the turbine (flow states at the bleed extraction are reproduced from the reports). In order to calculate appropriate fuel to air ratios, a combustor is included in the HPT performance model. Moreover, the HPT outlet conditions are applied as LPT inlet conditions. Since the performance models reproduce the available data of the NASA E3 design reports [9,10], they are suited for the calibration of the turbine disk design process.
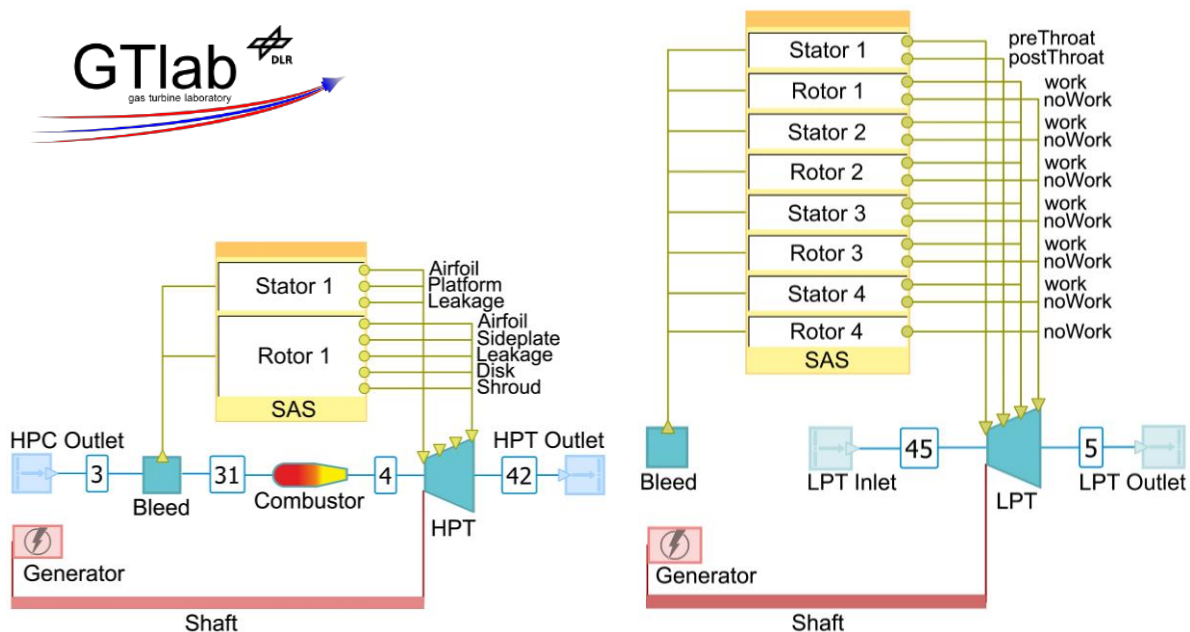

Figure 1 – Performance models of P&W's NASA E3 single-stage HPT and four-stage LPT.

Table 1 – Turbine performance data of P&W's NASA E3 HPT and LPT.

Parameter	Unit	HPT		LPT	
		CR (Design)	TO (Off-Design)	CR (Design)	TO (Off-Design)
$T_{t,in}$	K	1633	1713	1161	1226
P	MW	14.1	31.7	13.5	28.2
n	1/s	220.5	231.1	65.0	64.4
$p_{t,in}/p_{t,out}$	-	4.0	4.0	5.51	4.91
$\dot{m}_{SAS}/\dot{m}_{in}$	%	15.84	15.84	2.02	2.02

By using the GTlab predesign module, reference geometries are generated for the single-stage HPT and the four-stage LPT to represent the NASA E3 turbine cross-sections. These reference geometries are illustrated in Figure 2 and include the turbine annulus, disks and LPT shrouds which are an integral part of the LPT rotor blades. The flow path and blade row dimensions as well as the disk radii and thicknesses are reproduced from the NASA E3 design reports [9,10]. Note that the disk rim radius shown in Figure 2 corresponds to the radius at which the disk is no longer interrupted by blade root cavities (see also Figure 6).
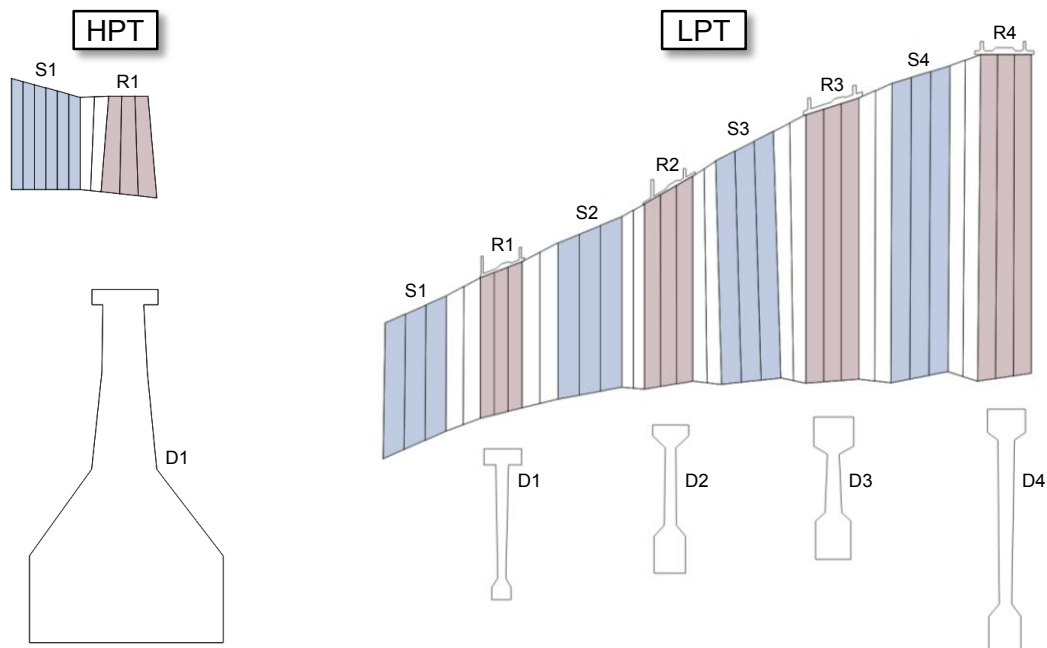

Figure 2 – Reference geometries of P&W's NASA E3 single-stage HPT and four-stage LPT reproduced from the design reports [9,10].

3. Knowledge-Based Geometry and Mass Estimation

An essential part of GTlab are the sketchpad and mass estimation modules offering the opportunity for knowledge-based conceptual geometry and mass prediction. Figure 3 summarizes the methodology; details of the entire process are provided in [15]. In summary, the geometry estimation is based on thermodynamic data provided by a performance model and dimensionless geometrical characteristics, such as blade aspect or taper ratio. The dimensionless characteristics are extracted from a reference geometry and inherently contain the knowledge of the engine technology. Once the knowledge-based sketching process is calibrated, the reference geometry is reproduced accurately.

Moreover, a comprehensive geometry model is generated, which can be visualized in a 2D or 3D plot. Finally, the mass is estimated based on the generated performance and geometry model as well as a material database provided by GTlab.
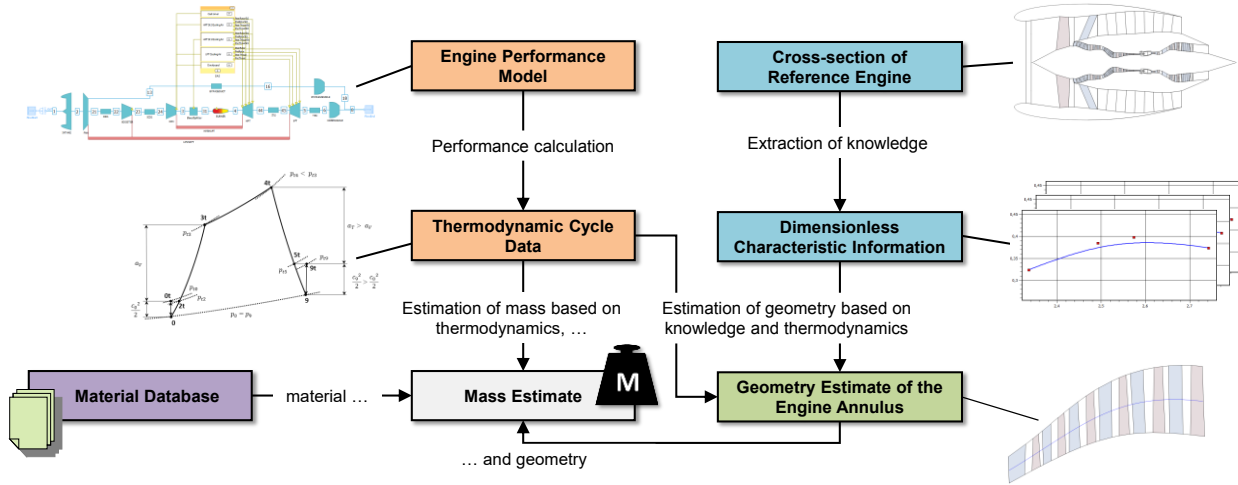

Figure 3 – Methodology of knowledge-based conceptual geometry and mass estimation [15].

As part of this paper, the described process is carried out for P&W's NASA E3 HPT and LPT. Figure 4 shows the 3D plot of the created turbine geometry models.
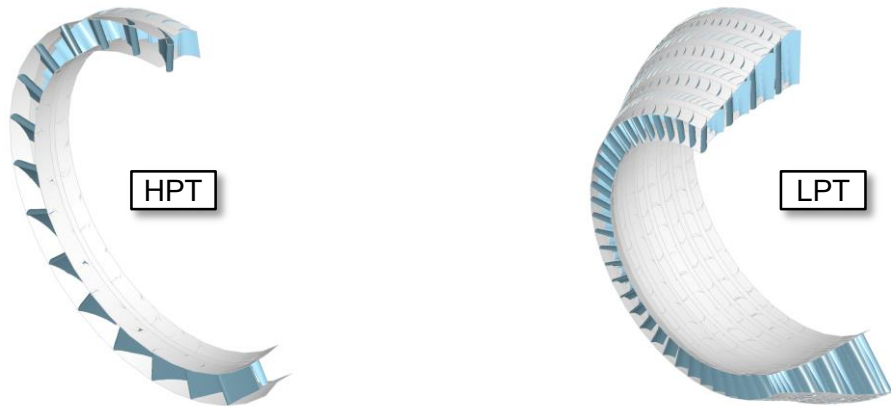

Figure 4 – 3D plot of the geometry models of P&W's NASA E3 single-stage HPT and four-stage LPT (LPT shrouds are not plotted).

The predicted blade masses m_{bl} are listed in Table 2 (note that the corresponding materials are included in Table 3). Solid airfoil masses $m_{af,sol}$ are calculated by the GTlab internal CAD kernel [16] based on the airfoil cross-sections plotted in the NASA E3 design reports [9,10]. In order to consider the cavities of cooled HPT airfoils, a cavity factor CF_{af} is applied that is estimated by means of the reported HPT airfoil cross-sections (see Eq. (1) and Eq. (2)). Since the LPT rotor blades are shrouded, shroud masses m_{sh} are added to the LPT rotor airfoil masses m_{af} which are also calculated by the GTlab internal CAD kernel according to the shroud reference geometries shown in Figure 2.

$$CF_{af} = V_{af,cav}/V_{bl,sol} \qquad (1)$$

$$m_{af} \approx m_{af,sol} \cdot \left(1 - CF_{af}\right) \qquad (2)$$

Table 2 – Turbine performance data of P&W's NASA E3 HPT and LPT.

| Parameter	HPT		LPT							
	S1	R1	S1	R1	S2	R2	S3	R3	S4	R4
NoB [-]	24	54	54	120	72	96	84	100	108	122
CF_{bl} [-]	60.4	42.8	0.0 (uncooled)							
m_{af} [kg]	4.5	3.8	9.4	6.4	13.9	8.6	18.7	15.5	29.3	21.8
m_{sh} [kg]	-	0.0	-	2.5	-	2.8	-	4.5	-	4.2
m_{bl} [kg]	4.5	3.8	9.4	8.9	13.9	11.4	18.7	20.0	29.3	26.0

4. Knowledge-Based Disk Modeling

In this section, the knowledge-based design process presented in section 3 is extended in order to incorporate turbomachinery disks. After the selection of suitable disk materials (see section 4.1), the knowledge-based modeling of disk geometries is focused (see section 4.2). Subsequently, the disk mass and material temperature are estimated (see section 4.3 and 4.4). Finally, a stress and burst analysis is performed to evaluate the structural disk integrity (see section 4.5 and 4.6).

4.1 Material Selection

In general, turbomachinery disks are produced by casting, forging or powder metallurgy (PM), whereby combinations of these processes are also possible [1,17,18]. The popularity of the PM route has grown steadily over the last decades and is now an essential manufacturing process for turbomachinery disks. The component materials used in this paper are presented in Table 3. Additionally, yield strength curves are provided, since the yield strength σ_y is an important parameter for structural turbomachinery disk analysis, as carried in this paper (see section 4.5). According to the NASA E3 design report [9], the HPT turbine disk is made of "advanced MERL 80", however, no information on this material is available. Therefore, Rene 95 is applied in this paper which was developed by GE in the 1970s and thus corresponds well to the technology level of the NASA E3 [19-21]. Rene 95 is processed primarily by PM, has a temperature capability up to 650 °C and is one of the strongest nickel-base superalloys for highly stressed disks. Compared to normal MERL 80 [22], Rene 95 provides a slightly higher yield strength curve and is consequently a suitable substitute for the unknown HPT alloy "advanced MERL 80" (see Table 3). For the LPT disks, MERL 76 is used which is an advanced high strength hot isostatic pressed (HIP) PM superalloy [10,23].

Table 3 – Materials used to model P&W's NASA E3 single-stage HPT and four-stage LPT including yield strength characteristics.

Turbine	Component	Material	
HPT	S1, R1	PWA 1484 [24]	
	D1	Rene 95 [20]	
LPT	S1	PWA 1484 [24]	
	S2, R1	MAR-M 247 [25]	
	S3, S4, R2, R3, R4	Inconel 713C [26]	
	D1, D2, D3, D4	MERL 76 (HIP) [23]	
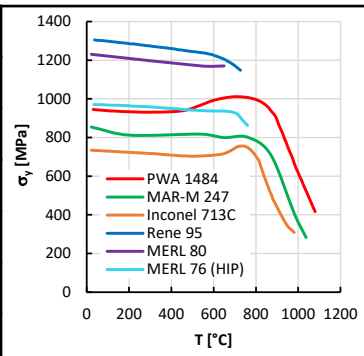
4.2 Geometry Modeling

After determining the turbine flow path and blade masses (see section 3), the next step is to model the blade root and disk geometries. A first tensile stress prediction of the rotors can be performed in advance, e.g. by evaluating the well-established parameter AN^2 [14, 27]. However, in this paper, it is assumed directly that the rotors withstand the occurring centrifugal forces, since the focus is on conceptual disk design and an already tested and constructed turbine is investigated. In the following step, engineers have to choose between a detailed blade root design or an initial disk design without extensive blade root analysis. Due to complex geometries, such as dovetail or fir tree, blade root modeling is a challenging task [28], but the portion of the blade roots in total engine weight is significantly lower than that of the disks (see Table 7). Consequently, direct disk design is an effective approach which is also pursued in this paper in terms of the knowledge-based geometry and mass estimation methodology presented in Figure 3.

A principle blade-disk assembly is illustrated in Figure 5. The blades are connected to the disk through the blade roots, whereby the toothing of the disk is referred to as the disk tang. This paper proposes to approximate the area of disk tang and blade root as a simplified annulus in order to be able to start directly with the intended disk modeling (see also Figure 6). Generally, the simplified root annulus represents the corresponding volume with sufficient accuracy; merely peripheral elements, such as parts of the blade root platform, could be outside of the annulus boundaries. The annulus size is dimensioned by the blade root width w_{rt} and the average blade root height $h_{rt,ave}$ which are transformed into dimensionless parameters by referring to the axial chord at the blade hub $c_{ax,hub}$. The annulus volume V_{an} is calculated by the GTlab internal CAD kernel [16]. By defining a blade root volume share Sh_{rt}, the annulus volume is split into the blade root volume V_{rt} and the disk tang volume V_{dt} (see Eq. (3)). Additionally, a cavity factor CF_{rt} is used to consider the blade root cavity volume V_{cav} (see Eq. (4)). Assuming equal blade root width w_{rt} and disk tang width w_{dt}, these parameters are determined using a representative cross-section (see Figure 5). After the volume computation, the corresponding masses are calculated based on the materials listed in Table 3.
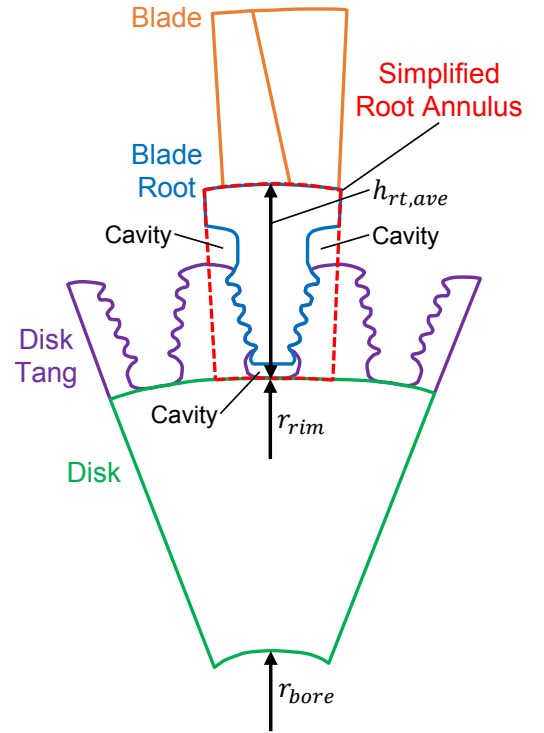

Figure 5 – Principle blade-disk assembly.

$$Sh_{rt} = \frac{V_{rt} + V_{rt,cav}}{V_{an}} = \frac{A_{rt} + A_{rt,cav}}{A_{ref}} \qquad (3)$$

$$CF_{rt} = \frac{V_{rt,cav}}{V_{rt} + V_{rt,cav}} = \frac{A_{rt,cav}}{A_{rt} + A_{rt,cav}} \qquad (4)$$

According to the knowledge-based geometry prediction illustrated in Figure 3, the described simplified root annuls parameters are extracted from the reference geometries (see Figure 2) as well as the NASA E3 design reports [9,10]. The results are presented in Table 4.

Table 4 – Knowledge-based simplified root annulus parameters.

Turbine		$h_{rt,ave}/c_{ax,hub}$ [-]	$w_{rt}/c_{ax,hub}$ [-]	Sh_{rt} [%]	CF_{rt} [%]
HPT	R1	1.71	1.19	72.0	17.1
LPT	R1	0.97	0.90	75.9	0.0
	R2	0.90	0.74		
	R3	0.73	0.74		
	R4	0.63	0.69		

After modeling the simplified root annulus, the rim radius r_{rim} and rim width w_{rim} are determined which provide the interface to the actual disk (see Figure 6). The rim radius is an important parameter because it indicates the border between dead and live weight. It has become established to consider the sum of blade mass m_{bl}, blade root mass m_{rt} and disk tang mass m_{dt} as dead mass m_{de}, whereas the disk mass m_{di} is refered to as live mass m_{li} [2-4]. Moreover, it is assumed that the dead weight causes the pull stresses on the rim of the live disk. Stresses are only absorbed in the live disk; the disk tang does not absorb any stresses according to the assumption made.
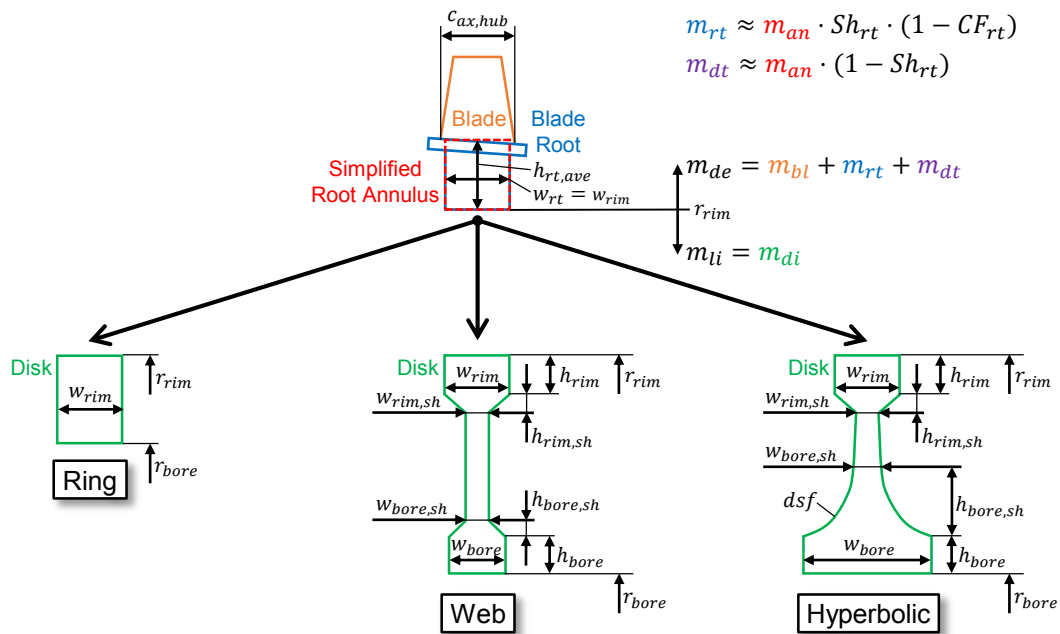

Figure 6 – Dead and live mass calculation and illustration of disk types with dimensions.

Basically, there are three different types of disks: ring, web and hyperbolic. The disk types and the corresponding dimensions are illustrated in Figure 6. Important parameter sets for the dimensionless parametrization of disk geometries are listed in Table 5, whereby it is presupposed that the rim radius r_{rim} and rim width w_{rim} are already known. Ring disks are simple to model, whereas web and hyperbolic disks require a more comprehensive data set. To approximate the curved part of symmetric hyperbolic disks, the so-called disk shape factor dsf is introduced additionally. By means of this factor, the radial thickness distribution of the disk is described as follows:

$$w(r) = \frac{w_{bore} - w_{bore,sh}}{(h_{bore,sh})^{dsf}} \cdot \left(r_{bore} + h_{bore} + h_{bore,sh} - r\right)^{dsf} + w_{bore,sh} \tag{5}$$

Furthermore, Table 5 provides typical disk applications. Web and hyperbolic disks are essential for HPTs and LPTs, whereas ring disks are mainly used in fans, low-pressure compressors (LPCs) or in the first stage of high-pressure compressors (HPCs) [4].

Table 5 – Parameter sets for dimensionless disk geometry parametrization and typical disk applications.

Disk Type	Ring	Web	Hyperbolic
Input	r_{rim}		
	w_{rim}		
General Disk Parameters	r_{bore}/r_{rim}	r_{bore}/r_{rim}	r_{bore}/r_{rim}
	-	w_{bore}/w_{rim}	w_{bore}/w_{rim}
Specific Disk Parameters	-	h_{rim}/w_{rim}	h_{rim}/w_{rim}
	-	$h_{rim,sh}/w_{rim}$	$h_{rim,sh}/w_{rim}$
	-	$w_{rim,sh}/w_{rim}$	$w_{rim,sh}/w_{rim}$
	-	h_{bore}/w_{bore}	h_{bore}/w_{bore}
	-	$h_{bore,sh}/w_{bore}$	$h_{bore,sh}/w_{bore}$
	-	$w_{bore,sh}/w_{bore}$	$w_{bore,sh}/w_{bore}$
	-	-	dsf
Application	Fan, LPC, 1st HPC stage	LPC, HPC, LPT	HPT

As part of this paper, the knowledge-based geometry and mass estimation methodology illustrated in Figure 3 is extended by the previously described disk modeling strategy. All disks are approximated as symmetric disks; in case of an asymmetric disk, an equivalent symmetric disk in modeled (by symmetric thickness distribution around the corresponding centerline). Table 6 presents the determined disk design parameters which are derived from the generated reference geometries of P&W's NASA E3 single-stage HPT and four-stage LPT (see Figure 2). Using the values listed in Table 6, the knowledge-based sketching process reproduces the reference geometries accurately. Since the HPT disk has almost no curvature in the bore shoulder area, the disk shape factor dsf is set to 1, which corresponds to a thick web disk. Figure 7 shows a 3D plot of the extended turbine geometry models including the generated simplified root annuli and disks. Furthermore, the disk geometries are provided in the appendix (see Figure 13).

Table 6 – Knowledge-based disk design parameters.

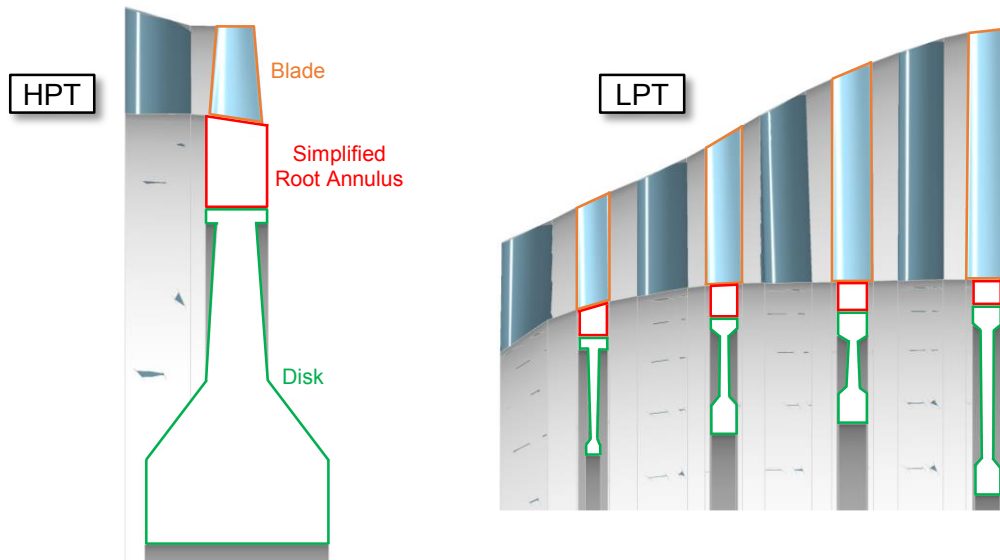| Parameter	HPT	LPT			
	D1	D1	D2	D3	D4
Disk Type	Hyperbolic	Web	Web	Web	Web
r_{bore}/r_{rim}	0.25	0.76	0.77	0.78	0.64
w_{bore}/w_{rim}	2.93	0.51	0.88	0.89	0.85
h_{rim}/w_{rim}	0.23	0.42	0.30	0.73	0.62
$h_{rim,sh}/w_{rim}$	0.00	0.00	0.33	0.20	0.20
$w_{rim,sh}/w_{rim}$	0.62	0.33	0.30	0.30	0.44
h_{bore}/w_{bore}	0.45	0.65	1.18	1.08	1.06
$h_{bore,sh}/w_{bore}$	0.45	0.46	0.36	0.24	0.39
$w_{bore,sh}/w_{bore}$	0.34	0.42	0.39	0.47	0.38
dsf	1	-	-	-	-

Figure 7 – 3D plot of the geometry models of P&W's NASA E3 single-stage HPT and four-stage LPT including simplified root annuli and disks (LPT shrouds are not plotted).

4.3 Mass Estimation

The rotor assembly mass estimation results are summarized in Table 7. Note that the corresponding materials are listed in Table 3 and that all masses are calculated by the GTlab internal CAD kernel [16] based on the generated knowledge-based turbine geometry models shown in Figure 7. As defined in Eq. (6), the rotor assembly mass m_{rotAss} is calculated by summing the masses of all rotating components per stage, such as rotor blade masses $m_{bl,i}$, rotor blade root masses $m_{rt,i}$, disk tang masses $m_{dt,i}$ and disk masses $m_{di,i}$. Additionally, the mass of rotating seals m_{seal} and, if present, the mass of a frame connected to the disks m_{frame} are considered.

$$m_{rotAss} = m_{seal} + m_{frame} + \sum \left(m_{bl,i} + m_{rt,i} + m_{dt,i} + m_{di,i}\right) \tag{6}$$

The predicted total rotor blade mass of the HPT amounts 29.2 kg and is close to the mass of 32.0 kg published in the HPT design report [9]. According to [28], the reported mass was calculated for solid rotor blades, however, hollow blades are considered in this paper, since such blades are also used in the actual turbine. If the mass estimation is carried out for solid rotor blades by setting the airfoil cavity factor CF_{af} to zero, a total rotor blade mass of 31.96 kg is computed which matches the literature value well. The mass for the disk and seals is stated in the HPT report as 150.0 kg [9]. In [28], a disk mass prediction was performed without seals and a total disk mass of 118.4 kg was published which agrees with the mass of 121.3 kg calculated in this paper. To determine the mass of the rotating seals, the live disk geometry is extended manually and all connected seals are incorporated as illustrated in Figure 8. Thus, a sealing mass of 31.3 kg is obtained, resulting in a total disk mass including seals of 152.6 kg. This value matches the literature value of 150.0 kg well, validating the disk geometry and mass modeling carried out in this paper.

Regarding the LPT, there are no other publications in the literature to date, so that only the original LPT design report [10] is used for comparison. The published rotor assembly mass amounts 381.8 kg, but the bookkeeping for the assembly is not clear and it seems that an A-frame is included. In this paper, a rotor assembly as shown in Figure 8 is assumed, leading to a rotor assembly mass of 348.2 kg. Compared to HPT, the deviation from the literature value is greater, but the deviation is still less than 10 %. Considering the uncertainties of the report and the simplified assumptions made, this is a reasonable result.

Table 7 – Rotor assembly mass estimation results.

Mass in [kg]		HPT	LPT			
		R1	R1	R2	R3	R4
Dead Mass	m_{bl}[a]	3.8	8.9	11.4	20.0	26.0
	m_{rt}	25.4	10.6	10.3	10.4	8.8
	m_{dt}	11.0	3.1	3.3	3.3	2.8
	m_{de}	40.2	22.6	25.0	33.7	37.6
Total Rotor Blade Mass	$m_{bl} + m_{rt}$	29.2	19.5	21.7	30.4	34.8
Live Disk Mass	$m_{li} = m_{di}$	110.3	15.7	21.9	28.8	34.5
Total Disk Mass	$m_{di} + m_{dt}$	121.3[b]	18.8	25.2	32.1	37.3
Sealing Mass	m_{seal}	31.3	65.8			
Total Disk + Sealing Mass	$m_{di} + m_{dt} + m_{seal}$	152.6[c]	191.7			
Frame Mass	m_{frame}	no frame	62.6			
Rotor Assembly Mass	m_{rotAss}	167.1	348.2[d]			

a) See also Table 2.
b) Comparable to mass estimation results in [28].
c) Comparable to mass estimation results in [9].
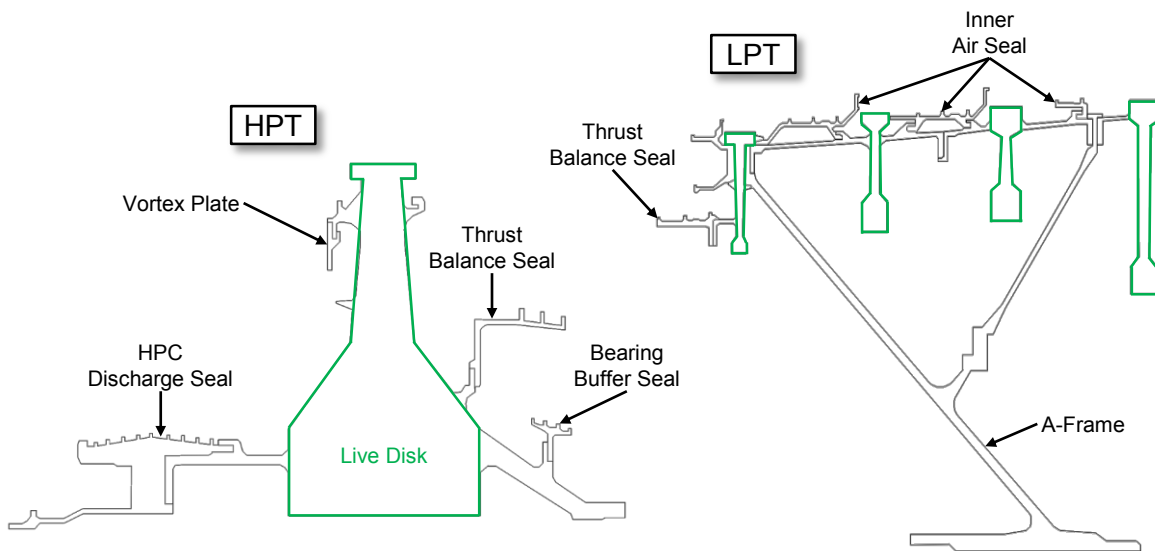d) Comparable to mass estimation results in [10].

Figure 8 – Extended live disk geometries including connected seals and frames used for mass estimation (the live disk extension mass is considered in the sealing mass of Table 7).

4.4 Temperature Estimation

An appropriate disk material temperature estimation is crucial, since the temperature has a significant impact on the material properties (see Table 3) as well as the occurring mechanical stresses (see section 4.5). Basically, the heat diffusion and thus the temperature distribution in a solid component is described by Fourier's heat equation. In the stationary case ($\partial T / \partial t = 0$), considered in this work, Fourier's heat equation results in Poisson's equation (see Eq. (7)) which includes the material thermal conductivity k and the volumetric heat source $\dot{q}_V$. Note that the thermal conductivity k is considered constant in Eq. (7).

$$k\nabla^2 T + \dot{q}_V = 0 \qquad (7)$$

In this paper, it is assumed that the temperature does not change in the circumferential and axial direction, leading to a one-dimensional heat diffusion equation. Based on this assumption, the following second order ordinary differential equation (ODE) results for an infinitesimal disk element at

the radius r after solving the Laplace operator ∇^2:

$$\frac{1}{r}\frac{\partial}{\partial r}\left(r\frac{\partial T}{\partial r}\right) + \frac{\dot{q}_V}{k} = 0 \tag{8}$$

Since the disk thickness t is a function of the radius r, it is not reduced in the derivation and has to be considered [29]:

$$\frac{1}{r}\frac{\partial}{\partial r}\left(rt\frac{\partial T}{\partial r}\right) + t\frac{\dot{q}_V}{k} = 0 \tag{9}$$

To calculate the resulting disk temperature distribution from the ODE shown in Eq. (9), the ODE is solved numerically by means of finite difference method. Therefore, the disk is divided into equidistant elements with a finite height Δr by a user-defined number of radial discretization points. The discretization applied in this paper is illustrated in Table 8. For all disks, 100 discretization points are used leading to 99 elements. As indicated by the relative element height Δr_{rel}, the disks are finely discretized, but the calculation is nevertheless rapid. Additionally, two boundary conditions have to be specified at the disk rim and bore radius to solve the ODE. In this work, the rim and bore temperature are predefined which can be reproduced from the NASA E3 design reports (see Figure 6.4-1 in [9] and Figure 5.2.1-18 in [10]). Finally, the described process is repeated in an outer loop with the calculated temperature distribution as input until the thermal conductivity k is converged in order to account for the temperature dependence of this material property.

Table 8 – Equidistant turbine disk discretization including schematically discretized disk.

Turbine		Discretization Points [-]	$\Delta r_{rel} = \frac{\Delta r}{r_{rim}-r_{bore}}$ [%]	
HPT	D1	100	1.0	
LPT	D1	100	1.0	
	D2			
	D3			
	D4			

To consider the convective heat transfer between the disk and the surrounding air cavities, the discretized volumetric heat source $\dot{q}_{V,discret}$ is used as suggested in [29] (see Eq. (10)). Note that h_{cav} is the cavity heat transfer coefficient which varies in radial direction. $A_{discret}$ is the front and rear surface connected to the surrounding cavities, $V_{discret}$ is the volume and $T_{discret}$ is the temperature of the respective discretized disk element. Furthermore, the total cavity temperature $T_{t,cav}$ is applied which is averaged between the front and rear side for simplification as illustrated in Figure 9.

$$\dot{q}_{V,discret} = \frac{\dot{Q}}{V_{discret}} = \frac{h_{cav}A_{discret}(T_{t,cav}-T_{discret})}{V_{discret}} \tag{10}$$

The cavity heat transfer coefficient h_{cav} in Eq. (10) is influenced by many factors, however, a proper estimate is required nonetheless. A common conceptual approach for heat transfer coefficient prediction is the use of Nusselt number correlations which are usually obtained from simulations or experiments. Based on the Nusselt number Nu, the cavity thermal conductivity k_{cav} and the local disk radius r, the cavity heat transfer coefficient h_{cav} is calculated as shown in Eq. (11). A Nusselt number correlation for rotating generic disks is presented in Eq. (12). Note that Re is the Reynolds number

and a is a correlation factor that has to be calibrated for each disk (see Figure 10). This correlation has been formulated in various publications [30-33] and is valid for fully turbulent flows with a Reynolds number greater than about 320000 (all disks investigated here are above this limit). The Reynolds number Re is determined as defined in Eq. (13) based on the local disk radius r, the angular velocity ω, the cavity density ρ_{cav} and the cavity dynamic viscosity μ_{cav}. Both the cavity thermal conductivity k_{cav} in Eq. (11) and the cavity dynamic viscosity μ_{cav} in Eq. (13) are calculated by means of VDI Heat Atlas polynomials for air [34]. The cavity density ρ_{cav} is estimated using the ideal gas law, whereby the total cavity temperature $T_{t,cav}$ (see Figure 9) and the total turbine inlet pressure are applied approximately.

$$h_{cav} = \frac{Nu \cdot k_{cav}}{r} \tag{11}$$

$$Nu = a \cdot Re^{0.8} \tag{12}$$

$$Re = \frac{\rho_{cav} \cdot u \cdot r}{\mu_{cav}} = \frac{\rho_{cav} \cdot \omega \cdot r^2}{\mu_{cav}} \tag{13}$$

Since the air temperature of the surrounding disk cavities significantly affects the resulting material temperature distribution through heat transfer (see Eq. (9) and Eq. (10)), cavity temperature modeling is crucial. This is particularly challenging for HPT disks which feature multiple cavities due to cooling air routing as well as sealing. For P&W's NASA E3 HPT and LPT considered here, it is possible to reproduce the cavity temperatures of each disk by means of the corresponding design reports (see Figure 6.4-1 in [9] and Figure 5.2.5-5 in [10]). The radial cavity temperature distribution of the HPT disk at TO conditions is illustrated in Figure 9 as a function of the relative disk radius r_{rel} defined in Eq. (14). The temperatures are plotted as difference to the total high-pressure compressor (HPC) outlet temperature $T_{t,3}$ which is the dominating temperature for HPT disks due to the cooling air extraction. Consequently, positive values indicate cooling air heating within the secondary air system (SAS), mainly caused by the combustor, whereas negative values imply cooling air extraction at a lower pressure level in the HPC. Obviously, a large portion of the disk front cavity air is hotter than $T_{t,3}$, except for the pre-swirl cavity highlighted in green and the bore cavity.

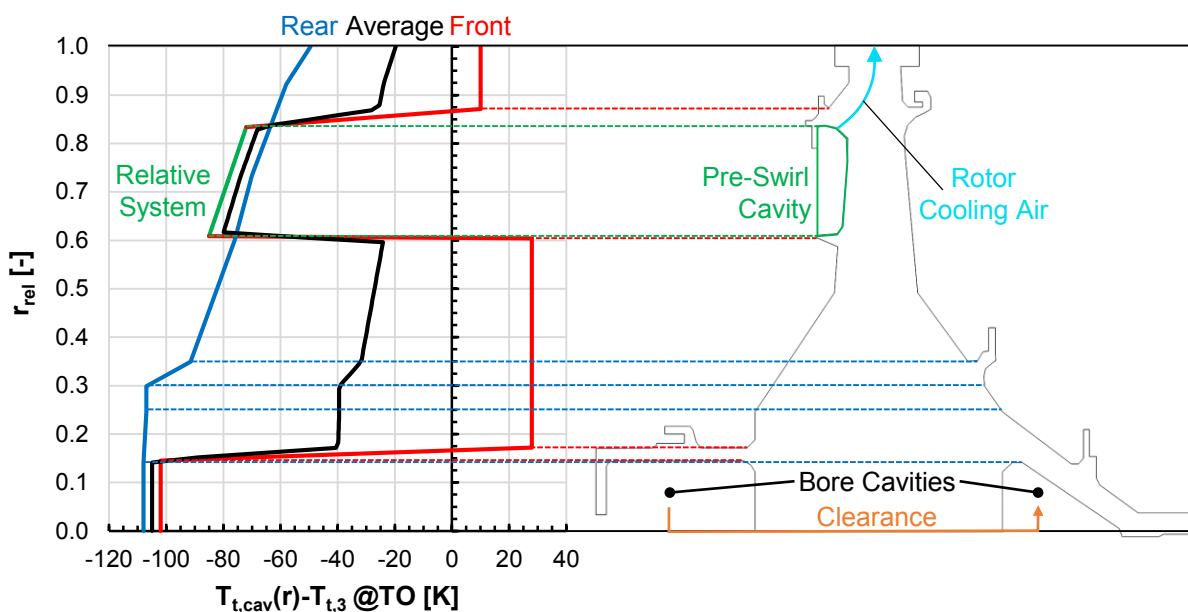$$r_{rel} = \frac{r - r_{bore}}{r_{rim} - r_{bore}} \tag{14}$$

Figure 9 – Disk cavity temperature distribution of P&W's NASA E3 HPT at TO conditions.

The air enters the pre-swirl cavity through the so-called pre-swirl nozzles which are used to generate a pre-swirl in order to ensure a swirl-free flow into the rotating disk. Afterwards, the air flows to the rotors to cool them. Since the air in the pre-swirl cavity is completely surrounded by rotating solid parts (see Figure 8), it is valid to consider the air in the relative system, leading to a reduction in the total cavity temperature $T_{t,cav}$ as shown in Figure 9 (note that this temperature drop is also included in Figure 6.4-1 of the NASA E3 HPT design report [9]). The air for the bore cavity is mainly extracted after the seventh HPC stage and is therefore significantly colder than $T_{t,3}$. From the front bore cavity, the air flows through a clearance between the disk and the shaft to the rear cavity (highlighted in orange in Figure 9), resulting in similar front and rear bore cavity temperatures. The air then heats up in radial direction on its path through the rear cavities to the main gas flow. In the course of the one-dimensional disk material temperature modeling followed in this paper (see Eq. (9) and Eq. (10)), an axial disk temperature change cannot be considered, so an average cavity temperature between disk front and rear side is applied as illustrated in Figure 9.

For the NASA E3 LPT disks, the determination of the cavity temperature is not as complex as for the HPT disk, since each LPT disk rotates entirely in a single cavity (see Figure 8). Consequently, no radial subdivision of the cavity temperature distribution is required. Based on Figure 5.2.5-5 of the NASA E3 LPT design report [10], the following values result for the temperature difference between the total cavity temperature $T_{t,cav}$ and the total HPC outlet temperature $T_{t,3}$ at TO conditions: -61 K for the first, second and third disk and -74 K for the fourth disk.

Since the cavity temperature distributions are appropriately modeled (see Figure 9), the disk thermal conductivity is given in the literature (see Table 3) and the NASA E3 design reports contain the real disk material temperature distributions (see Figure 6.4-1 in [9] and Figure 5.2.5-5 in [10]), it is possible to calibrate the Nusselt correlation factor a introduced in Eq. (12). Figure 10 presents the calibrated disk material temperature distributions for PW's NASA E3 HPT and LPT at TO conditions. The temperatures are plotted as difference to the disk bore temperature $T(r_{bore})$ so that the temperature increase in radial direction is visible. By using a Nusselt correlation factor of a = 0.006 for the HPT, the reported disk material temperature is reproduced accurately. Moreover, it is apparent that the pre-swirl nozzle causes a temperature drop in the upper disk part (see also Figure 8 and Figure 9). Regarding the LPT, only a few literature values are available for the first disk, but it is nevertheless possible to calibrate the Nusselt correlation factor to a = 0.031. The material temperature distributions of the other LPT disks are qualitatively adjusted, the corresponding Nusselt correlation factors are provided in Figure 10.
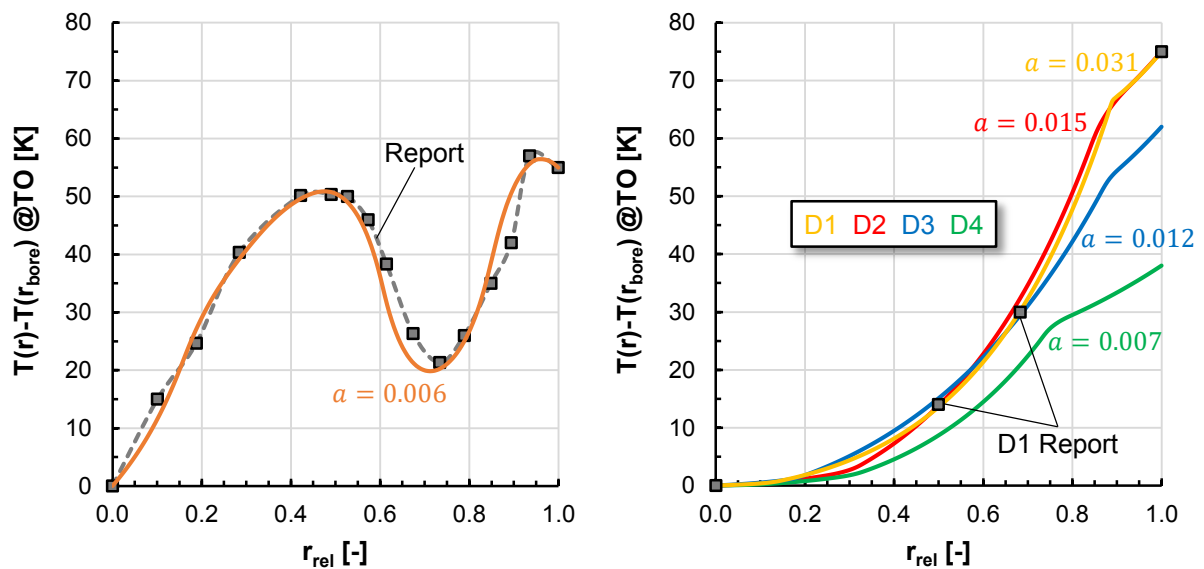

Figure 10 – Disk material temperature distribution of P&W's NASA E3 HPT (left) and LPT (right) at TO conditions.

To the authors' knowledge, the disk material temperature prediction presented in this section and its calibration to the NASA E3 HPT and LPT is novel in the literature. The approach is specially tailored to turbine disks and their conceptual design. By analyzing the secondary air system and the cooling air extraction positions, it is possible to provide a first estimate of the disk cavity temperature already in the early phase of conceptual design. The use of Nusselt number correlations enables a preliminary assessment of the heat transfer coefficient.

4.5 Stress Analysis

After disk geometry modeling (see section 4.2) and valid mass prediction (see section 4.3) of all rotating components as well as a realistic disk material temperature estimation (see section 4.4), it is necessary to perform a first conceptual stress analysis in order to evaluate the structural integrity of the disks. Based on an infinitesimal disk element with the thickness t at the radius r, the following differential equation is derived by calculating the force equilibrium in radial direction (where σ_r is the radial stress and σ_t the tangential stress) [2,3]:

$$\frac{d}{dr}(tr\sigma_r) - t\sigma_t + t\rho\omega^2 r^2 = 0 \tag{15}$$

Moreover, the radial strain ε_r and tangential strain ε_t results from the infinitesimal disk element by analyzing the kinematic relationships (note that v is Poisson's ratio, E is the modulus of elasticity and α thermal expansion coefficient):

$$\varepsilon_r = \frac{1}{E}(\sigma_r - v\sigma_t) + \alpha(T - T_{ref}) \tag{16}$$

$$\varepsilon_t = \frac{1}{E}(\sigma_t - v\sigma_r) + \alpha(T - T_{ref}) \tag{17}$$

Eq. (16) and Eq. (17) are transformed in order to solve for the radial stress σ_r and tangential stress σ_t:

$$\sigma_r = \frac{E}{1-v^2}\left[\varepsilon_r + v\varepsilon_t - (1+v)\alpha(T - T_{ref})\right] \tag{18}$$

$$\sigma_t = \frac{E}{1-v^2}\left[\varepsilon_t + v\varepsilon_r - (1+v)\alpha(T - T_{ref})\right] \tag{19}$$

The strains in the polar system are related to the radial displacement u as follows:

$$\varepsilon_r = \frac{du}{dr} \tag{20}$$

$$\varepsilon_t = \frac{u}{r} \tag{21}$$

Inserting Eq. (20) and Eq. (21) into Eq. (18) and Eq. (19) results in:

$$\sigma_r = \frac{E}{1-v^2}\left[\frac{du}{dr} + v\frac{u}{r} - (1+v)\alpha(T - T_{ref})\right] \tag{22}$$

$$\sigma_t = \frac{E}{1-v^2}\left[\frac{u}{r} + v\frac{du}{dr} - (1+v)\alpha(T - T_{ref})\right] \tag{23}$$

In this paper, the radial stress σ_r and tangential stress σ_t are calculated according to Eq. (22) and Eq. (23). Furthermore, Eq. (22) and Eq. (23) indicate that the radial stress σ_r and tangential stress σ_t are a function of the radial displacement u which is still unknown. To calculate the radial displacement, Eq. (22) and Eq. (23) are inserted into Eq. (15), leading to a second order ODE which only contains the radial displacement u as an unknown (detailed information on the ODE is provided in the appendix of [29]). Using finite difference method, the ODE is solved numerically to determine the radial displacement u (note that the same discretization is applied as shown in Table 8). Additionally, two boundary conditions have to be specified at the disk rim and bore radius in order to

solve the ODE (see Eq. (24)). The dead mass centrifugal force causes the tensile stress at the rim radius, whereas the bore radius is treated as stress-free [3]. Table 7 lists the dead masses used in this work and the rim radial stress is approximated by smearing the dead mass centrifugal force around the disk rim circumference.

$$\sigma_r = \begin{cases} \dfrac{m_{de}r_{de}\omega^2}{2\pi r_{rim}w_{rim}} & at \ r_{rim} \\[2ex] 0 & at \ r_{bore} \end{cases} \tag{24}$$

Once the radial displacement u has been computed numerically, the radial stress σ_r and tangential stress σ_t are determined for each discretized disk element according to Eq. (22) and Eq. (23). Based on these stresses, the von Mises stress σ_{vM} is calculated as follows:

$$\sigma_{vM} = \sqrt{{\sigma_r}^2 + {\sigma_t}^2 - \sigma_r\sigma_t} \tag{25}$$

The relation of the yield strength σ_y of the material used (see Table 3) to the von Mises stress σ_{vM} results in the disk safety factor SF that is used to evaluate the structural integrity of the disk in the early phase of conceptual design (see Eq. (26)). It is a common practice to consider a safety factor SF greater than one in order to ensure a sufficient margin for uncertainties and physical effects that have not been modeled yet (e.g. lifetime-limiting failure modes such as low cycle fatigue or creep). Otherwise, a disk failure is to be expected. *Armand* [2] recommends a disk safety factor of SF = 1.1.

$$SF = \frac{\sigma_y}{\sigma_{vM}} \tag{26}$$

Figure 11 and Figure 12 present the disk stress and safety factor results for P&W's NASA E3 HPT and LPT at TO conditions. The HPT stress distribution shows exemplarily that the tangential stress σ_t is significantly greater than the radial stress σ_r and thus dominates the von Mises stress σ_{vM}. Besides, the stresses are greatest at the disk bore radius (r_{rel} = 0) which is consequently the critical radius for the disk design.

It is possible to validate the stress results by comparing the average tangential stresses $\sigma_{t,ave}$ with the values provided by the NASA E3 design reports [9,10]. Table 9 proves that reasonable agreement is achieved, especially considering the uncertainties related to the reports and the simplified assumptions made in this paper. The deviations are less than 5 %, apart from the third LPT disk with 13.8 %. The first LPT disk is not analyzed anymore, as the stress here is significantly higher than the literature value. This is probably due to the fact that the disk is connected to the A-frame in reality and is therefore more stress-resistant (see Figure 8). However, this connection cannot be modeled, since the conceptual design methods presented in this paper only support the mechanical evaluation of the live disk. Without the A-frame, the live disk has an unconventional web geometry and the thin bore part is a main reason for the high stresses.

The safety factor curve of the NASA E3 HPT disk indicates that this component is highly stressed (see Figure 11). At the bore radius (r_{rel} = 0), the safety factor is even 0.96, but a safety factor of 1.0 is already reached in the next discrete disk element (r_{rel} = 0.01). Generally, a safety factor of less than one is not permissible, however, it is a very sensitive parameter and can also become greater than one if the assumed boundary conditions or material properties change slightly. Additionally, the safety factor is greater than unity over a wide range and the average tangential stresses is met accurately (see Table 9). Therefore, falling below the safety factor limit at the bore radius is acceptable in the scope of this paper, but a safety factor greater than one is mandatory when designing disks for a new turbomachinery. Accordingly, the safety factor of 1.1 suggested by *Armand* [2] is an appropriate estimate for HPT disks. Compared to the HPT, the analyzed LPT disks are subjected to significantly lower stresses. The minimum safety factors at the bore radius (r_{rel} = 0) are between 1.29 and 1.38 and thus above the recommendation of *Armand* [2].
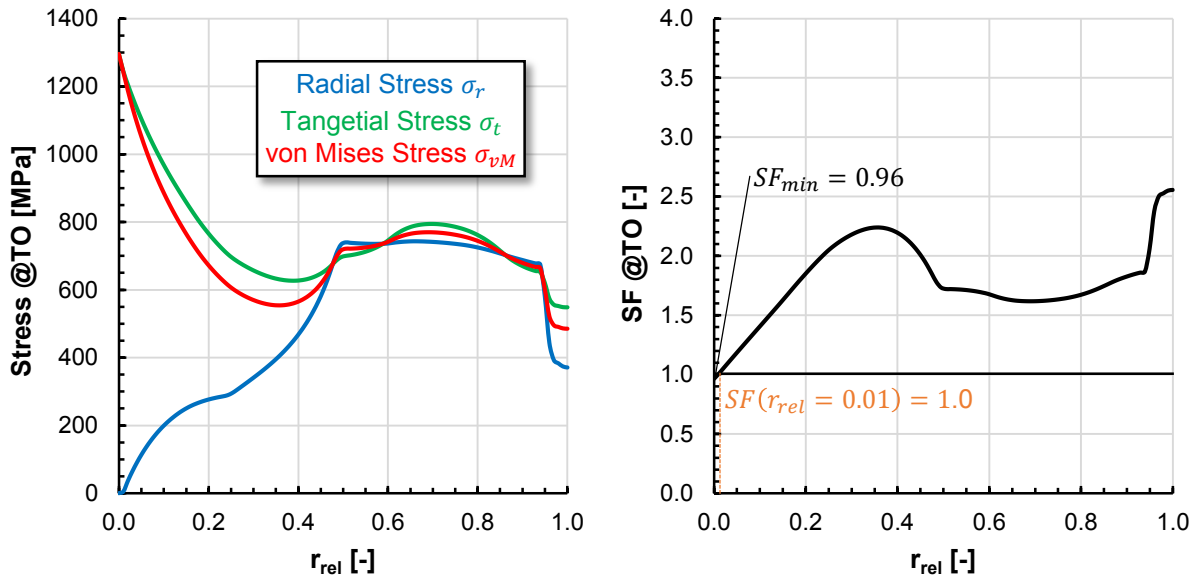
Figure 11 – Disk stress distribution and safety factor of P&W's NASA E3 HPT at TO conditions.
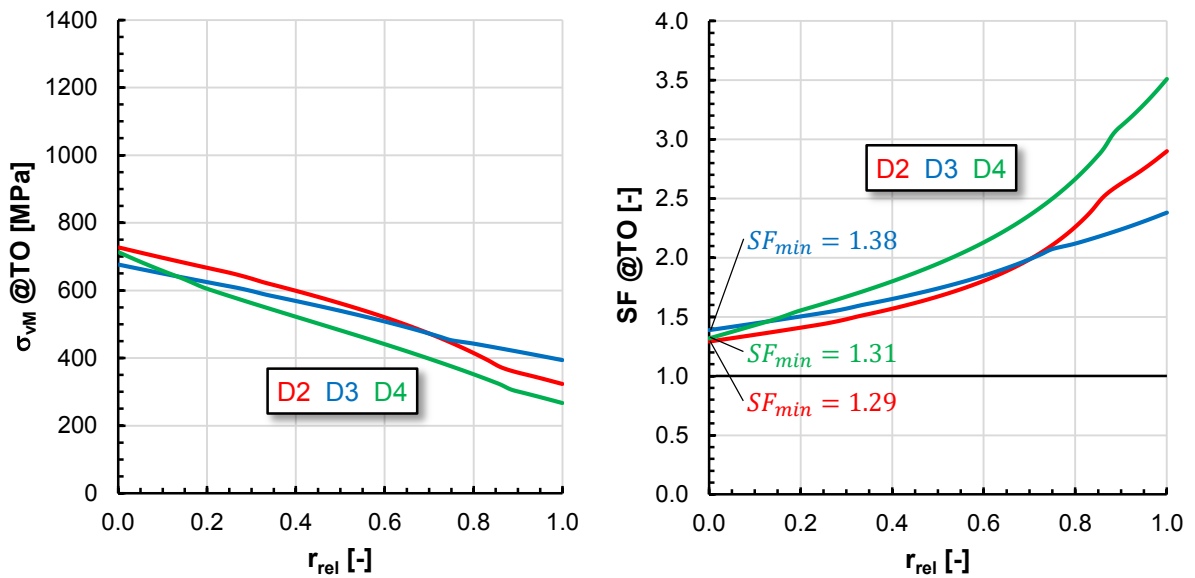

Figure 12 – Disk von Mises stresses and safety factors of P&W's NASA E3 LPT at TO conditions.

Table 9 – Average tangential stress compression with NASA E3 design reports [9,10] at TO conditions.

Turbine	Disk	$\sigma_{t,ave}$ [MPa]	$\sigma_{t,ave,report}$ [MPa]	Deviation [%]
HPT	D1	759	796 [9]	-4.6
LPT	D1	-	434 [10]	-
	D2	579	585 [10]	-1.0
	D3	562	652 [10]	-13.8
	D4	523	550 [10]	-4.9

4.6 Burst Analysis

Turbomachinery disk burst is a worst-case scenario and must be avoided at all costs [35]. Consequently, a sufficient safety margin against disk burst should already be considered in the early phase of the conceptual design [6,36,37]. One important parameter is the burst margin BM (see Eq. (27)) which is calculated by relating the ultimate tensile strength (evaluated at the average disk temperature) $\sigma_u(T_{ave})$ to the average tangential stresses $\sigma_{t,ave}$ listed in Table 9 [3,38]. Moreover, a burst safety factor SF_{BM} is included in Eq. (27), whereby a value of SF_{BM} = 0.47 is proposed by *Tong et al.* [3].

$$BM = SF_{BM} \frac{\sigma_u(T_{ave})}{\sigma_{t,ave}} \tag{27}$$

In order to estimate the available burst speed margin n_{burst}/n (see Eq. (28)), it is possible to use a simple correlation that is referred to several times in the literature [36,37,38]. Note that n is the maximum speed at which the disk stresses are evaluated.

$$\frac{n_{burst}}{n} = \sqrt{\frac{\sigma_u(T_{ave})}{\sigma_{t,ave}}} \tag{28}$$

A more advanced approach to calculate the burst speed margin was introduced by GE (see Eq. (29)), also called the Hallinan criterion [6,36,37]. In addition to further terms related to the maximum tangential stress $\sigma_{t,max}$, the notch strength ratio NSR is considered which is a material parameter [20].

$$\frac{n_{burst,GE}}{n} = 0.95 \left[\frac{1}{NSR} \left(\sqrt{\frac{\sigma_u(T_{ave})}{\sigma_{t,ave}}} - \sqrt{\frac{\sigma_u(T_{ave})}{\sigma_{t,max}}} \right) + \sqrt{\frac{\sigma_u(T_{ave})}{\sigma_{t,max}}} \right] \tag{29}$$

Since the burst margin BM is provided for each disk in the NASA E3 design reports [9,10], the ultimate tensile strength σ_u is given in the literature (see Table 3) and the average tangential stress $\sigma_{t,ave}$ is matched accurately (see Table 9), it is possible to calibrate the burst safety factor SF_{BM} according to Eq. (27). Table 10 presents the calibration results and the safety factors are close together in a range between 0.55 and 0.59. Apparently, the value of SF_{BM} = 0.47 proposed by *Tong et al.* [3] is relatively optimistic and could result in a design with low safety against disk burst. Again, the first LPT disk is not considered anymore, as the connection to the A-frame cannot be modeled mechanically (see Figure 8 and section 4.5).

Furthermore, the burst speed margin n_{burst}/n is listed in a Table 10 for each disk which is calculated based on Eq. (28) and Eq. (29), respectively. For the disks investigated here, the burst speed estimation introduced by GE (Hallinan criterion [6,36,37]) leads to more conservative results and thus offers more safety in the design process. All burst speed margins are above 130 %, the lower limit specified in [38]. If the Federal Aviation Administration (FAA) [39] or European Union Aviation Safety Agency (EASA) [40] certification guidelines on rotor integrity are considered, rotors must withstand a maximum of 120 % overspeed. Accordingly, the disks must also guarantee a burst speed margin of at least 120 % in order to avoid burst failure.

Table 10 – Burst safety factor calibration based on the NASA E3 design reports [9,10] and burst speed margins at TO conditions.

Turbine	Disk	BM [-]	SF_{BM} [-]	n_{burst}/n [-]	$n_{burst,GE}/n$ [-]
HPT	D1	1.22 [9]	0.58	1.45	1.32
LPT	D1	1.66 [10]	-	-	-
	D2	1.43 [10]	0.59	1.55	1.44
	D3	1.36 [10]	0.55	1.57	1.47
	D4	1.48 [10]	0.55	1.64	1.51

5. Conclusion

In this paper, a conceptual design process for turbomachinery disks is proposed which is demonstrated and calibrated using the NASA Energy Efficient Engine (E3). Performance and geometry models are generated for the single-stage high-pressure turbine (HPT) and four-stage low-pressure turbine (LPT) of the NASA E3. The first step is the definition of a suitable disk parameterization in order to extend a knowledge-based geometry modeling process. Subsequently, the masses of all rotating components are predicted based on the generated geometries and a reasonable agreement with the literature values is achieved. The deviation regarding the total rotor assembly mass is 1.7 % for the HPT and 8.8 % for the considerably heavier LPT. Disk material temperatures are estimated using a novel approach tailored for turbine disks that considers the heat transfer between the disk and the surrounding cavities. Therefore, a Nusselt number correlation for rotating disks is applied, whose correlation factor is calibrated by means of the created NASA E3 models. Furthermore, a stress and burst analysis is performed to evaluate the structural disk integrity. Average tangential stresses are compared to the literature values, validating the stress calculation. The deviations are less than 5 %, apart from the third LPT disk with 13.8 %. Finally, the safety factors used in stress and burst analysis are assessed. For HPT disks, the yield strength safety factor of 1.1 suggested in the literature is an appropriate estimate. Burst safety factors are calibrated for each disk according to the reported burst margins and range between 0.55 and 0.59.

6. Acknowledgements

7. Contact Author Email Address

Patrick Wehrel

German Aerospace Center (DLR)

Institute of Propulsion Technology

Cologne, Germany

mailto: patrick.wehrel@dlr.de

8. Copyright Statement

References

[1]   Reed, R. C. Superalloys for Turbine Disc Applications in *The Superalloys - Fundamentals and Applications*. 1. Edition, Cambridge University Press, Cambridge, 2006.

[2]   Armand, S. C. *Structural Optimization Methodology for Rotating Disks of Aircraft Engines*. NASA Technical Memorandum, NASA-TM-4693, 1995.

[3]   Tong, M. T., Halliwell, I. and Ghosn, L. J. A Computer Code for Gas Turbine Engine Weight and Disk Life Estimation. *Journal of Engineering for Gas Turbines and Power*, Vol. 126, No. 2, pp. 265-270, 2004.

[4]   Gutzwiller, D. P. and Turner, M. G. Rapid Low Fidelity Turbomachinery Disk Optimization. *Advances in Engineering Software*, Vol. 41, No. 5, pp. 779–791, 2010.

[5]   Kolias, I. et al. A Tool for the Design of Turbomachinery Disks for an Aero-Engine Preliminary Design Framework. *Aerospace*, Vol. 10, No. 5, 2023.

[6] Barack, W. N. and Domas, P. A. *An Improved Turbine Disk Design to Increase Reliability of Aircraft Jet Engines*. General Electric Report, NASA CR-135033, 1976.

[7] Bisset, J. W. and Howe, D. C. *NASA Energy Efficient Engine - Flight Propulsion System Preliminary Analysis and Design Report - Final Update*. Pratt & Whitney Report, NASA CR-174701, 1983.

[8] Ciepluch, C. C., Davis, D. Y. and Gray, D. E. Results of NASA's Energy Efficient Engine Program. *Journal of Propulsion and Power*, Vol. 36, pp. 560–568, 1987.

[9] Thulin, R. D., Howe, D. C. and Singer, I. D. *NASA Energy Efficient Engine - High-Pressure Turbine Detailed Design Report*. Pratt & Whitney Report, NASA CR-165608, 1982.

[10] Leach, K., Thulin, R. D. and Howe, D. C. *NASA Energy Efficient Engine - Turbine Intermediate Case and Low-Pressure Turbine Component Test Hardware Detailed Design Report*. Pratt & Whitney Report, NASA CR-167973, 1982.

[11] Reitenbach, S. et al. Collaborative Aircraft Engine Preliminary Design using a Virtual Engine Platform, Part A: Architecture and Methodology. *AIAA SciTech 2020 Forum*, Orlando (Florida), 2020.

[12] Wehrel, P. and Carvalho, F. Cooling Model Calibration in a Collaborative Turbine Preliminary Design Process Using the NASA Energy Efficient Engine - Part I: 0D Performance Modeling. *13th International Gas Turbine Congress*, Kyoto (Japan), 2023.

[13] Carvalho, F. et al. Cooling Model Calibration in a Collaborative Turbine Preliminary Design Process Using the NASA Energy Efficient Engine - Part II: 1D Turbine Modeling. *13th International Gas Turbine Congress*, Kyoto (Japan), 2023.

[14] Walsh, P. P. and Fletcher, P. *Gas Turbine Performance*. 2. Edition, Blackwell Science, Oxford, 2004.

[15] Häßy, J. and Schmeink, J. Knowledge-Based Conceptual Design Methods for Geometry and Mass Estimation of Rubber Aero Engines. *33rd Congress of the International Council of the Aeronautical Sciences*, Stockholm, 2022.

[16] Siggel, M. et al. Closing the Gap between Data Model driven Geometry Generation and HiFi CAD for Automatized and Consistent Design Analysis. *AIAA SciTech 2024 Forum*, Orlando (Florida), 2024.

[17] McTiernan, B. J. Powder Metallurgy Superalloys in *ASM Handbook Powder Metallurgy*. ASM International, Ohio, 2015.

[18] Yang, L. et al. Status and Development of Powder Metallurgy Nickel-Based Disk Superalloys. *International Journal of Materials Research*, Vol. 101, No. 10, pp. 901-910, 2019.

[19] Engineering Alloys Digest. Datasheet Rene 95 Alloy. *Alloy Digest*, Vol. 23, No. 4, 1974.

[20] Kattus, J. R. Rene 95 in *Aerospace Structural Metals Handbook*. 1996.

[21] Wilbers, L. G. and Redden, T. K. *Powder Metallurgy René 95 Rotating Turbine Engine Parts*. General Electric Report, NASA CR-165142, 1981.

[22] Evans, D. J. *Evaluation of Powder Metallurgy Superalloy Disk Materials*. Pratt & Whitney Report, NASA CR-134865, 1975.

[23] Eng, R. D. and Evans, D. J. *Hot Isostatically Pressed Manufacture of High Strength MERL 78 Disk and Seal Shapes*. Pratt & Whitney Report, NASA CR-165549, 1982.

[24] Cetel, A. D. and Duhl, D. N. Second-Generation Nickel-Base Single Crystal Superalloy. *Superalloys*, pp. 235–244, 1988.

[25] Kaufman, M. Properties of Cast Mar-M-247 for Turbine Blisk Applications. *Superalloys*, pp. 43-52, 1984.

[26] Nickel Institute. *Engineering Properties of Alloy 713C - A Practical Guide to the Use of Nickel-Containing Alloys*. https://www.nickelinstitute.org/media/4686/ni_inco_337_engineering713.pdf, 28.05.2024.

[27] Mattingly, J. D. and Heiser, W. H. *Aircraft Engine Design*. 2. Edition, American Institute of Aeronautics and Astronautics, Inc., Reston (Virginia), 2002.

[28] Bretschneider, S. *Knowledge-Based Preliminary Design of Aero-Engine Gas-Generators*. Dissertation, University of Stuttgart, Institute of Aircraft Propulsion Systems, 2011.

[29] Vieweg, M. *Integration der transienten Leistungssyntheserechnung in den multidisziplinären Vorentwurfsprozess.* Dissertation, Ruhr University Bochum, 2022.

[30] Owen, J. M., Haynes, C. M. and Bayley, F. J. Heat Transfer from an Air-Cooled Rotating Disk. *Proceedings of the Royal Society of London*, Vol. 336, No. 1607, pp. 453-473, 1974.

[31] Popiel, Cz. O. and Bogusławski, L. Local Heat-Transfer Coefficients on the Rotating Disk in Still Air. *International Journal of Heat and Mass Transfer*, Vol. 18, No. 1, pp. 167-170, 1975.

[32] Maccallum, N. R. L. Transient Expansion of the Components of an Air Seal on a Gas Turbine Disc. *SAE Aerospace Meeting*, Los Angeles (California), 770974, 2023.

[33] Cardone, G., Astarita, T. and Carlomagno, G. M. Heat Transfer Measurements on a Rotating Disk. *International Journal of Rotating Machinery*, Vol. 3, No. 1, pp. 1-9, 1997.

[34] Verein Deutscher Ingenieure (VDI). *VDI Heat Atlas*. 2. Edition, Springer, Berlin, Heidelberg, 2010.

[35] Xuan, H. et al. Containment of High-Speed Rotating Disk Fragments. *Journal of Zhejiang University SCIENCE A*, Vol. 13, No. 9, pp. 665-673, 2012.

[36] Chianese, S. *Safety Factor Against Burst Speed of Turbomachinery Rotating Disks.* Master Thesis, University of Illinois, 2013.

[37] Xie, Y. et al. Burst Speed Prediction and Reliability Assessment of Turbine Disks: Experiments and Probabilistic Aspects. *Engineering Failure Analysis*, Vol. 145, 2023.

[38] Kurzke, J. *GasTurb Details 6*. 1. Edition, GasTurb GmbH, Aachen (Germany), 2021.

[39] Legal Information Institute (LII). *14 CFR § 33.27 - Turbine, Compressor, Fan, and Turbosupercharger Rotor Overspeed*. https://www.law.cornell.edu/cfr/text/14/33.27, 28.05.2024.

[40] European Union Aviation Safety Agency (EASA). CS-E 840 in *Certification Specifications and Acceptable Means of Compliance for Engines (CS-E)*. Amendment 5, EASA, Cologne (Germany), 2018.
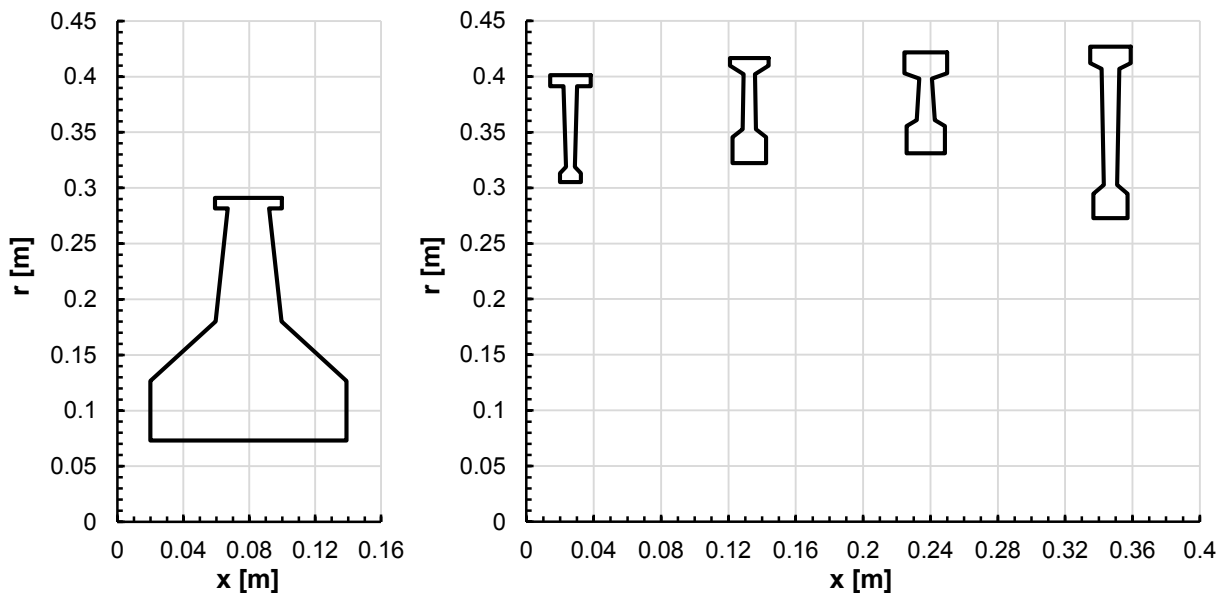
Appendix

Figure 13 – Disk geometries of P&W's NASA E3 single-stage HPT (left) and four-stage LPT (right) generated by knowledge-based sketching.